

Timescales of Quasar Accretion Discs from Low to High Black Hole Masses and new Variability Structure Functions at the High Masses

Christian Wolf^{1,2}  *, Samuel Lai³ , Ji-Jia Tang^{1,4} , John Tonry⁵ 

¹Research School of Astronomy and Astrophysics, Australian National University, Cotter Road, Weston Creek ACT 2611, Australia

²Centre for Gravitational Astrophysics (CGA), Australian National University, Building 38 Science Road, Acton ACT 2601, Australia

³Commonwealth Scientific and Industrial Research Organisation (CSIRO), Space & Astronomy, P. O. Box 1130, Bentley, WA 6102, Australia

⁴Graduate Institute of Astrophysics and Department of Physics, National Taiwan University, No. 1, Sec. 4 Roosevelt Road, Taipei 10617, Taiwan

⁵Institute for Astronomy, University of Hawaii, 2680 Woodlawn Drive, Honolulu, HI 96822-1897, U.S.A.

Accepted XXX. Received YYY; in original form ZZZ

ABSTRACT

The UV-optical variability of quasars appears to depend on black-hole mass M_{BH} through physical timescales in the accretion disc. Here, we calculate mean emission radii, R_{mean} , and orbital timescales, t_{orb} , of thin accretion disc models as a function of emission wavelength from 1 000 to 10 000 Å, M_{BH} from 10^6 to 10^{11} solar masses, and Eddington ratios from 0.01 to 1. At low M_{BH} , we find the textbook behaviour of $t_{\text{orb}} \propto M_{\text{BH}}^{-1/2}$ alongside $R_{\text{mean}} \approx \text{const}$, while towards higher masses the growing event horizon imposes $R_{\text{mean}} \propto M_{\text{BH}}$ and thus a turnover into $t_{\text{orb}} \propto M_{\text{BH}}$. We fit smoothly broken power laws to the numerical results and provide analytic convenience functions for $R_{\text{mean}}(\lambda, M_{\text{BH}}, L_{3000})$ and $t_{\text{orb}}(\lambda, M_{\text{BH}}, L_{3000})$ in terms of the observables λ , M_{BH} , and the monochromatic luminosity L_{3000} . We then calculate variability structure functions for the $\sim 2\,200$ brightest quasars in the sky with estimates for M_{BH} and L_{3000} , using lightcurves from NASA/ATLAS orange passband spanning more than 7 years. The median luminosity of the accretion disc sample is $\log L_{\text{bol}}/(\text{erg s}^{-1}) \approx 47$ and the median $\log M_{\text{BH}}/M_{\odot} \approx 9.35$. At this high mass, the theoretical mass dependence of disc timescales levels off and turns over. The data show a weak dependence of variability on M_{BH} consistent with the turnover and a model where disc timescale drives variability amplitudes in the form $\log A/A_0 = 1/2 \times \Delta t/t_{\text{orb}}$, as suggested before. In the future, if the black-hole mass is known, observations of variability might be used as diagnostics of the physical luminosity in accretion discs, and therefore constrain inclination or dust extinction.

Key words: galaxies: active – quasars: general

1 INTRODUCTION

The emission from accretion discs in Active Galactic Nuclei (AGN) is variable on all time scales (for reviews see Ulrich et al. 1997; Peterson 2001; Lawrence 2016). It is thus routinely observed in all classes of AGN, where our view of the accretion disc is not obscured, and even used as a signature to identify AGN in time-domain sky surveys (e.g. Palanque-Delabrouille et al. 2011). More importantly, characteristic behaviour within the seemingly stochastic variability is seen as a diagnostic tool to decipher physical properties of the discs. Sizes of accretion discs, e.g., are probed with disc reverberation analysis (e.g. Sergeev et al. 2005; Cackett et al. 2007; Jiang et al. 2017; Homayouni et al. 2019; Yu et al. 2020), although there are also useful and complementary non-variability tools such as SED fitting (e.g. Malkan 1983; Laor 1990; Calderone et al. 2013; Campitiello et al. 2018; Lai et al. 2023). AGN accretion discs are also promising candidates for standardisable candles to extend studies of cosmology to the highest redshifts beyond the easy reach of other probes such as type-Ia supernovae (Risaliti & Lusso 2019), and these studies would benefit from improved understanding of intrinsic disc properties.

Intriguingly, the physical origin of the stochastic variability in AGN is not yet agreed upon (e.g. Jiang & Blaes 2020; Neustadt & Kochanek 2022), and thus it is not clear what behaviour to expect and how it relates to physical properties. A plausible candidate for intrinsic instabilities in the disc is turbulence from magneto-rotational instability (MRI; Balbus & Hawley 1991), although it is not yet established that this would predict the observed levels of variability in the integrated light of a whole disc. Separately, the disc is expected to respond to heating from a variable X-ray corona, although a limited energy budget suggests that this is not the principal origin of UV-optical variability in AGN discs (e.g. Uttley et al. 2003; Secunda et al. 2024). At present, we are far from a view of disc variability that is grounded in first-principles understanding and verifiable in numerical simulations, although attempts at the latter are getting ambitious (Secunda et al. 2024), raising hope for future progress.

On the observational side, current progress in the quest to identify mechanisms behind the variability centres on parametric descriptions of the stochastic behaviour, in the search for order parameters in a likely complex process (e.g. Lawrence & Papadakis 1993; Edelson & Nandra 1999; McHardy et al. 2005). Common descriptions of the observed variability involve either the structure function (SF), most often for optical light curves (e.g. Vanden Berk et al. 2004; MacLeod et al. 2010; Kozłowski 2016), or the power spectral density (PSD),

* E-mail: christian.wolf@anu.edu.au

most often for X-ray light curves (e.g. [Lawrence & Papadakis 1993](#); [Paolillo et al. 2023](#)), although the opposite combinations exist as well (e.g. [Arévalo et al. 2024](#)). A common description for the stochastic variability uses the damped random-walk paradigm (e.g. [Kelly et al. 2009](#); [MacLeod et al. 2010](#)), where specific interest is focused on the slope and amplitude of the SF or PSD as well as breaks in slopes and their characteristic time scales.

Initially, scaling behaviour of the X-ray PSD has been primarily related to black-hole mass (e.g. [Lawrence & Papadakis 1993](#); [Edelson & Nandra 1999](#); [McHardy et al. 2005](#); [Kelly et al. 2013](#)); the optical behaviour in larger samples has been argued to be physically rooted in thermal fluctuations ([Kelly et al. 2009](#)). On the UV-optical side, increasingly large and reliable data sets have triggered too many independent studies to list them all (see above, but also including [Zuo et al. 2012](#); [Morganson et al. 2014](#); [Caplar et al. 2017](#); [Li et al. 2018](#); [Stone et al. 2022](#); [Arévalo et al. 2024](#)), and have greatly helped to refine our view of scaling behaviour. E.g., [Burke et al. \(2021\)](#) suggest that a long-term damping time scale of the optical variability scales with black-hole mass as well; [Tang et al. \(2023\)](#) find that the rest-frame UV structure function is universal when clocks are run in units of thermal or orbital timescale that depends on wavelength and disc luminosity. [Arévalo et al. \(2024\)](#) consider specifically the black-hole mass dependence in the orbital timescale of UV emission.

However, black-hole mass estimates are still quite uncertain, and calculations of physical timescales in an accretion disc may be even less trusted as they are model-dependent. While a standard model for thin accretion discs exists ([Shakura & Sunyaev 1973](#); [Novikov & Thorne 1973](#)), disc reverberation experiments and microlensing observations have suggested that the size scale of QSO discs may be off by a factor of ~ 3 ; however, the literature has not yet found agreement on a profound mismatch of disc sizes with the standard model, and recent works are questioning whether the signals seen in disc reverberation experiments are representing a propagating heat wave from the X-ray corona at all, rather than measuring an altogether different phenomenon ([Secunda et al. 2024](#)); if so, the latter might still be correlated with disc size, such that the search for size ratios relative to the standard model may not question the model but rather constrain a different mechanism behind temperature waves travelling in the disc ([Neustadt & Kochanek 2022](#)).

When observed features are related to orbital or thermal timescales in the accretion discs, there are also slightly different approximating definitions used. Straightforward analytic equations are based on simple Newtonian forces in circular orbits and idealised gas properties (for a handy summary in practical units, see e.g. [Kelly et al. 2013](#)). Based on a universal temperature profile of $T(R) \propto R^{-3/4}$ in the outer parts of a standard disc and idealised black-body emission, analytic solutions were obtained that express the timescales as a function of bolometric luminosity L_{bol} and the restframe wavelength λ_{rest} of observed light; [Morgan et al. \(2010\)](#), e.g., find an approximation for the disc scale length of $R \propto \lambda_{\text{rest}}^{4/3} M_{\text{BH}}^{2/3} (L_{\text{bol}}/L_{\text{Edd}})^{1/3}$, implying orbital and thermal time scales to follow $t \propto L_{\text{bol}}^{1/2} \lambda_{\text{rest}}^2$ independent of black-hole mass. Finally, scaling relations are fit to numerical calculations of disc emission profiles, most recently by [Arévalo et al. \(2024\)](#), who find a mass-dependent time scale of $t_{\text{orb}} \propto M^{0.65} R_{\text{Edd}}^{0.35}$ or $\propto M^{0.3} L_{\text{bol}}^{0.35}$ (while observing at a single restframe wavelength of $\lambda_{\text{rest}} \approx 290$ nm). Clearly then, interpretations of scaling behaviour depend on approximations used in scale definitions, which is good reason for further investigation of what approximations work well in which part of parameter space.

Another question concerns which are “fundamental parameters”, apart from an obvious dependence on the observing wavelength;

the suggestion implicit in [Morgan et al. \(2010\)](#) is L_{bol} , while many others prefer a combination of black-hole mass M_{BH} and the Eddington ratio $R_{\text{Edd}} = L_{\text{bol}}/L_{\text{Edd}} \propto L_{\text{bol}}/M_{\text{BH}}$. The latter combination has obviously an extra parameter to accommodate more complex behaviour, but whether L_{bol} or R_{Edd} should be given preference is less obvious – while they are trivially related and thus seemingly interchangeable, the question is whether behaviour turns out to be independent of one but dependent on the other as a result of what is truly a causal dependence on black-hole mass.

The practical use of these parameters in the analysis of real data is also challenged by their large measurement uncertainties. Black-hole mass is by far mostly estimated from virial methods in single-epoch spectra, where it comes with an uncertainty of ~ 0.5 dex ([Dalla Bontà et al. 2020](#); [Bennert et al. 2021](#)). L_{bol} is usually not observed but inferred from monochromatic luminosity with a standard bolometric correction (BC) that assumes that every AGN has the same spectrum ([Richards et al. 2006](#); [Runnoe et al. 2012](#)). While the UV-optical SEDs of most AGN appear largely uniform, it has been an obvious expectation that black holes of the largest mass will create the largest holes in the accretion discs and thus come with the coolest and reddest discs ([Laor & Davis 2011](#)) that should have the smallest bolometric correction. Indeed, the most luminous QSOs appear to be powered by black holes with over 10^{10} solar masses and are consistent with BC factors that are $\sim 3\times$ lower (e.g. [Lai et al. 2023](#); [Wolf et al. 2024](#)) than the standard values suggested for average QSOs ([Richards et al. 2006](#)). Therefore, when standard BCs are used, L_{bol} will be biased by M_{BH} . R_{Edd} is then a ratio obtained from a noisy M_{BH} and an L_{bol} estimate that is biased in the high- M_{BH} regime.

It would be surely more pleasing if more robust observables could be used in parametrising accretion discs. The changes we adopt in this paper are to work with observed luminosity directly instead of the noisier Eddington ratio and replace the mass-biased L_{bol} estimates with a more immediately observed monochromatic luminosity such as L_{3000} or L_{2500} , where subscripts refer to wavelength in Ångström; either one is ideally inferred from spectral decomposition, with the former commonly published in QSO catalogues (e.g. [Rakshit et al. 2020](#)) and the latter more often used in studies of X-ray-to-UV relations (e.g. [Liu et al. 2021](#)). This might seem like a small gain, given that an estimate of a monochromatic luminosity will depend not only on the accretion rate \dot{M} of the black hole alone but also on the viewing angle of the non-isotropically emitting accretion disc, on any dust extinction by the AGN host galaxy or nuclear material, and also on the black-hole spin. At least the spin dependence is lower than for L_{bol} and the BC factor is removed, which depends on M_{BH} and \dot{M} . Further to that, the simple standard model ignores any Comptonisation of radiation from the inner disc and the complexities of photospheres in what will not be ideal thin discs. While this may instill broad scepticism about taking any analysis of scaling behaviour too far, we may still optimistically attempt to quantify all possible effects in an ideal model and compare to observations. Here, it would be desirable if more capable and broadly accessible codes for calculating the spectra of thin and slim accretion discs such as `kerrbb` ([Li et al. 2005](#)) and `s1imbh` ([Sadowski 2011](#); [Straub et al. 2011](#)), respectively, came with an option of outputting radially resolved emission profiles.

As we now move into the era of big data on AGN variability, as facilitated by the Legacy Survey of Space and Time (LSST; [Ivezic et al. 2008](#)) starting soon at the Vera C. Rubin Observatory, we will wish to control for as many parameters in our interpretation of variability patterns, and ideally use a combination of variability and other diagnostics such as SED fitting (e.g. [Laor 1990](#); [Campitiello et al. 2018](#); [Lai et al. 2023](#)) and emission-line features (e.g. [Shen & Ho 2014](#); [Marziani et al. 2018](#); [Mejía-Restrepo et al. 2018](#)) to enlarge

the number of constraints on the physical parameters of black-hole mass M_{BH} , spin a , viewing angle i and accretion rate \dot{m} , with a view to breaking remaining degeneracies, from which we currently suffer.

In this paper then, we investigate the disc sizes and time scales and re-assess some of the choices made for their approximation. We will incorporate an approximate handling of General Relativity (GR) effects, and thus evaluate the dependence of time scales on the parameters $(L_{3000}, M_{\text{BH}}, \lambda_{\text{rest}}, a)$. In Section 2, we describe our calculations of disc properties and choices of GR approximation. In Section 3, we present the results at face value and re-use analytic arguments to predict dominant simple approximations for the behaviour. As we confirm where the simple approximations apply, it will become clear that the influence of black-hole mass depends heavily on the mass regime itself. The results are used in Section 4 to motivate a new parametrised approximation of the numerical grid, which can be used in future studies. In Section 5, we will then investigate whether a mass effect can be empirically seen in the data of QSOs with high-mass black holes from Tang et al. (2023) and to what extent it matches expectations worked out here.

2 DISC CALCULATION AND CHARACTERISATION

2.1 Description of calculations

Here, we describe our calculations for characteristic size scales and time scales of accretion discs in the thin-disc model. We use a temperature profile together with black-body emission spectra to evaluate radial emission profiles for different wavelengths. From these, we derive total disc luminosities as well as a light-weighted radius and light-weighted orbital and thermal time scales.

We start with the standard Newtonian temperature profile of geometrically thin, optically thick high-viscosity discs, as specified by Frank et al. (2002):

$$T_{\text{N}}^4(R) = \frac{3GM_{\text{BH}}\dot{M}}{8\pi R^3\sigma} \left[1 - \left(\frac{R_{\text{ISCO}}}{R} \right)^{1/2} \right], \quad (1)$$

where σ represents the Stefan-Boltzmann constant and R denotes the radial distance from the centre. R_{ISCO} is the innermost stable circular orbit (ISCO) of the black hole as determined by the black hole spin. We calculate three cases for $r_{\text{ISCO}} = R_{\text{ISCO}}/R_{\text{S}}$ with values of (1.5, 3, 4.5), with the Schwarzschild radius $R_{\text{S}} = 2GM_{\text{BH}}/c^2$; these correspond to spin values of $a = (+0.78, 0, -1)$.

We then apply approximate corrections for GR effects: for the emission spectrum, we follow the prescription of Hanawa (1989), which combines gravitational redshift and time dilation effects into the modified temperature profile of

$$\begin{aligned} T_{\text{GR}}(R) &= \sqrt{1 - \frac{3R_{\text{S}}}{2R}} T_{\text{N}}(R) \\ &= \sqrt{1 - \frac{3GM_{\text{BH}}}{Rc^2}} \left\{ \frac{3GM_{\text{BH}}\dot{M}}{8\pi R^3\sigma} \left[1 - \left(\frac{R_{\text{ISCO}}}{R} \right)^{1/2} \right] \right\}^{1/4}. \end{aligned} \quad (2)$$

We choose to neglect the frame-dragging (Lense-Thirring) effect, since we are dealing with sizes much larger than the black hole ergosphere. We also ignore relativistic beaming effects, which become relevant near the inner edge of the disc.

For any photon frequency ν and disc annulus at radius R , we create a radial annular flux density profile $F_{\nu}(R)$ as seen by an observer at

luminosity distance D by following Frank et al. (2002) and using

$$F_{\nu}(R) = \frac{4\pi h\nu^3 \cos i}{c^2 D^2} \frac{RdR}{e^{h\nu/kT(R)} - 1}, \quad (3)$$

where h is the Planck constant and k the Boltzmann constant. We then characterise the overall disc by calculating the bolometric luminosity as well as a monochromatic luminosity at $\lambda = 3000\text{\AA}$, L_{3000} . We integrate over the range of inclination angles (with an average $\cos i$ factor of $1/2$) and the radial extent of the disc, using

$$L_{3000} = 4\pi D^2 \int_{R_{\text{ISCO}}}^{R_{\text{out}}} F_{3000}(R), \quad (4)$$

where $F_{3000}(R)$ represents $F_{\nu}(R)$ at $\lambda_{\text{rest}} = 3000\text{\AA}$ and R_{out} denotes the outer edge of the disc. Given the wavelength range of interest in this work beyond just a monochromatic luminosity, we generally choose R_{out} as the disc radius at 500K, where we have surely captured the vast majority of thermal disc emission. In realistic AGN, we expect dust formation below temperatures of around 1000 to 1500 K, which means that the exact choice of outer cutoff for the disc will matter less than the complexity of real AGN and their deviation from ideal thin-disc models. From L_{3000} , we derive a fiducial *estimated* bolometric luminosity $L_{\text{bol,est}} = f_{\text{BC}} \times \lambda L_{3000}$ with $f_{\text{BC}} = 5.15$ (Richards et al. 2006) as commonly done.

Separately, we calculate a *true* bolometric luminosity L_{bol} , where we integrate the disc model $F_{\nu}(R)$ over relevant ranges in photon frequency to capture over 99% of the thermal disc emission, using

$$L_{\text{bol}} = 4\pi D^2 \int_{\nu_{\text{lo}}}^{\nu_{\text{hi}}} \int_{R_{\text{ISCO}}}^{R_{\text{out}}} F_{\nu}(R) d\nu, \text{ with } \cos i = 1/2 \text{ again,} \quad (5)$$

where ν_{lo} and ν_{hi} are frequencies corresponding to wavelength range of $\log(\lambda_{\text{rest}}/\text{\AA}) = [2, 4.1]$. The Eddington ratio can be calculated from Equation 5:

$$R_{\text{Edd}} = L_{\text{bol}}/L_{\text{Edd}} \quad (6)$$

where the Eddington luminosity is

$$L_{\text{Edd}} = \frac{GM_{\text{BH}}m_{\text{p}}c}{\sigma_{\text{T}}}, \quad (7)$$

using the proton mass m_{p} and the Thomson scattering cross-section for the electron, σ_{T} . We note that for $\log M_{\text{BH}} = 9$ and $\log R_{\text{Edd}} = 0$ we find $\log L_{\text{bol}}/(\text{erg s}^{-1}) = 47.097$ and $\log L_{3000}/(\text{erg s}^{-1} \text{\AA}^{-1}) = 42.908$; the difference of 4.189 dex is the factor $f_{\text{BC}} \times 3000 \text{\AA}$.

From the radial emission profiles, we determine flux-weighted mean emission radii, R_{mean} , for different wavelengths, assuming for simplicity a face-on view of the disc ($\cos i = 1$) and thus using

$$R_{\text{mean}} = \frac{\int_{R_{\text{ISCO}}}^{R_{\text{out}}} R F_{\nu}(R)}{\int_{R_{\text{ISCO}}}^{R_{\text{out}}} F_{\nu}(R)}. \quad (8)$$

Finally, we calculate a flux-weighted orbital time scale, t_{mean} , for different wavelengths from the radial emission profile. Here, we start from a Newtonian definition of the orbital period, $t_{\text{orb,N}}$, given by

$$t_{\text{orb,N}} = 2\pi \sqrt{\frac{R^3}{GM_{\text{BH}}}} \approx 101.26 \left(\frac{M_{\text{BH}}}{10^8 M_{\odot}} \right) \left(\frac{R}{100 R_{\text{S}}} \right)^{3/2} \text{ days} \quad (9)$$

and add the GR time dilation effect with the modification

$$t_{\text{orb}} = t_{\text{orb,N}} / \sqrt{1 - \frac{3R_{\text{S}}}{2R}}. \quad (10)$$

Note, that the t_{orb} in Kelly et al. (2013) is normalised $\sim 2.7\%$ larger than our $t_{\text{orb,N}}$, which, however, works out to be the same as our

t_{orb} for $R \simeq 30R_{\text{S}}$ (including GR effects). The mean flux-weighted orbital time scale is thus

$$t_{\text{mean}} = \frac{\int_{R_{\text{ISCO}}}^{R_{\text{out}}} t_{\text{orb}} F_{\nu}(R) dR}{\int_{R_{\text{ISCO}}}^{R_{\text{out}}} F_{\nu}(R) dR}. \quad (11)$$

Since thermal time scales are just viscosity-dependent multiples of the orbital time scale, we choose to proceed only with the more uniquely determined orbital time scale.

Overall, we explore a disc parameter space that covers the parameter ranges of $\log(\lambda_{\text{rest}}/\text{\AA}) = [3; 4]$, $\log(M_{\text{BH}}/M_{\odot}) = [6; 11]$, and $\log(R_{\text{Edd}}) = [-2; 0]$. In terms of black-hole spins, we explore three values, $a = -1$ (maximum retrograde spin), $a = 0$ (Schwarzschild black hole), and $a = +0.78$ (a high prograde spin).

These calculations determine the isotropically averaged luminosity of an accretion disc, while the luminosity measured for observed discs will depend on inclination. We also ignore inclination-dependent GR effects, which lead to second-order modifications of the spectral shape, the observed luminosity, and the mean scales.

2.2 Building an intuition

To first order, the discs in our model are black-body emitters with a common temperature profile, that form a 1-parameter family with a size scale R_{ref} for a fixed temperature T_{ref} as ordering parameter. But the complete family of temperature profiles in Eq. 2 is given by

$$\frac{T^4}{T_{\text{ref}}^4} = \frac{R_{\text{ref}}^3}{R^3} \frac{1 - \sqrt{\frac{R_{\text{ISCO}}}{R}}}{1 - \sqrt{\frac{R_{\text{ISCO}}}{R_{\text{ref}}}}} \quad (12)$$

and has the additional free parameter $R_{\text{ISCO}}/R_{\text{ref}}$. A 1-parameter subfamily of scaled identical temperature profiles is obtained when both edges of the disc, the inner edge $R_{\text{in}} = R_{\text{ISCO}}$ and the outer edge R_{out} , scale linearly with R_{ref} . If we define the outer edge by a fixed temperature T_{out} , where the disc ceases to contribute to the UV-optical emission due to low temperature, then $R_{\text{out}}/R_{\text{ref}}$ will be automatically constant given the fixed $T(R/R_{\text{ref}})$ profile. Requiring $R_{\text{ISCO}}/R_{\text{ref}} = \text{const}$ demands $M_{\text{BH}} \propto R_{\text{ref}}$. This 1-parameter family has spectra of identical shape, a mean surface luminosity at any wavelength that is constant across the whole family, and monochromatic and bolometric luminosities that scale as $L \propto R_{\text{ref}}^2$. This family of discs then also has constant values of $R_{\text{ref}}/\sqrt{L_{3000}}$, $M_{\text{BH}}/\sqrt{L_{3000}}$, $R_{\text{mean}}/\sqrt{L_{3000}}$ and $t_{\text{mean}}/\sqrt{L_{3000}}$.

The second parameter, $R_{\text{ISCO}}/R_{\text{ref}}$, covers the variation of the inner disc edge, which affects the inner temperature and emission profile and thus the spectral energy distribution, the mean surface luminosity, and bolometric correction. It also varies the inner edge of the disc integration and flux-weighted averaging; instead of the intuitive $R_{\text{ISCO}}/R_{\text{ref}}$, the second parameter could be chosen to be interchangeably $R_{\text{ref}}/\sqrt{L_{3000}}$, $M_{\text{BH}}/\sqrt{L_{3000}}$, or $R_{\text{mean}}/\sqrt{L_{3000}}$. As we shall see below, $t_{\text{mean}}/\sqrt{L_{3000}}$ could not be a unique second parameter; also, t_{mean} not only depends on the integration limits set by R_{ISCO} and thus on a combination of M_{BH} and black-hole spin a , but additionally depends on M_{BH} itself via the Keplerian orbits.

3 MODEL RESULTS

We first use the single wavelength of $\lambda_{\text{rest}} = 3000 \text{ \AA}$ from the grid of discs without black-hole spin to explore the dependence of the light-weighted radius scale R_{mean} and orbital time scale t_{mean} on black-hole mass, luminosity, and Eddington ratio; we will also

differentiate between the true λ -integrated bolometric luminosity L_{bol} and the monochromatic luminosity L_{3000} that is a common proxy for the bolometric luminosity through simple scaling with a BC factor. Specifically by looking at the mass dependence of the disc size and orbital time scales at fixed luminosity, we will find that it follows not one power law but a smoothly broken power law as the driving factor for the scale changes from low mass to high mass. We will compare the results from the numerical grid with simple analytic approximations and then develop an improved approximation.

3.1 Simple scaling approximations for size and time scales

In Figure 1, we show the mass dependence of the size scale (top row) and the orbital time scale (bottom row) while colour-coding the discs with Eddington ratios (left panels) and luminosities (centre and right panels). We see the 2-parameter family of discs squeezed into a narrow distribution of size scales proportional to black-hole mass, such that a power law index can easily be fitted. The approximation by [Morgan et al. \(2010\)](#),

$$R_{\text{mean}} \propto M^{2/3} R_{\text{Edd}}^{1/3} \propto M^{1/3} L_{\text{bol}}^{1/3}, \quad (13)$$

predicts $R_{\text{mean}} \propto M^{2/3}$ at fixed Eddington ratio and $R_{\text{mean}} \propto M^{1/3}$ at fixed luminosity L_{bol} . A slope of $2/3$ (dashed line, top left panel) fits the general trend in Figure 1. How an observed sample of QSOs will behave on average, depends on trends of Eddington ratio with black-hole mass. From observations of a small number of microlensed quasars, [Morgan et al. \(2010\)](#) found $R_{\text{mean}} \propto M^{0.8}$ (although, e.g., [Shen et al. \(2008\)](#) present a more elaborate study).

Following [Morgan et al. \(2010\)](#) further, the orbital time scale is $t_{\text{orb}} \propto M^{1/2}$ at fixed Eddington ratio and independent of mass at fixed L_{bol} . The mass slope of $1/2$ (dashed line, bottom left panel) fits the trend, as does the fit to similar calculations by [Arévalo et al. \(2024\)](#) who found $t_{\text{orb}} \propto M^{0.65}$ (solid line, bottom left panel). The spread around any fit is wider than that of the size scales (at fixed mass $t_{\text{orb}} \propto R^{3/2}$) and a curvature beyond a power law is more noticeable. While the second parameter can be captured with a scaling with Eddington ratio, the slope of a power-law fit to the latter depends on black-hole mass. A mean slope at fixed mass of $t_{\text{orb}} \propto R_{\text{Edd}}^{1/3}$ as predicted by the [Morgan et al. \(2010\)](#) approximation is similar to the [Arévalo et al. \(2024\)](#) fit of $t_{\text{orb}} \propto R_{\text{Edd}}^{0.35}$.

The middle panels of Figure 1 render the same points colour-coded by luminosity L_{bol} . The mass dependence of the scales is generally weaker when evaluated at fixed L rather than fixed $R_{\text{Edd}} \propto L/M$ due to the intrinsic additional factor M . The dashed lines with the [Morgan et al. \(2010\)](#) slopes of $1/3$ (top centre panel) and 0 (bottom centre panel) are now meant to follow the distribution of points in one colour, not the overall distribution. The [Arévalo et al. \(2024\)](#) fit translates into $t_{\text{orb}} \propto M_{\text{BH}}^{0.3}$, but the [Morgan et al. \(2010\)](#) solution seems at least as acceptable. However, the evident relation is still not a single power law but shows curved behaviour. We note, that this is the true L_{bol} as determined by integrating over all emission; in practice, L_{bol} is often estimated from a monochromatic luminosity with a standard mass-independent bolometric correction factor. Thus, we ought to consider the relation between t_{mean} and L_{3000} as a proxy for a commonly estimated $L_{\text{bol,est}}$.

The right panels of Figure 1 render the same points colour-coded by luminosity L_{3000} , which we prefer as a more robust observable when considering a wide range of black-hole masses. Here, we find that the numerically calculated t_{mean} declines with increasing mass at fixed L_{3000} in the low-mass regime, then shows a parabolic turnover at intermediate masses and finally increases with mass at high black-hole

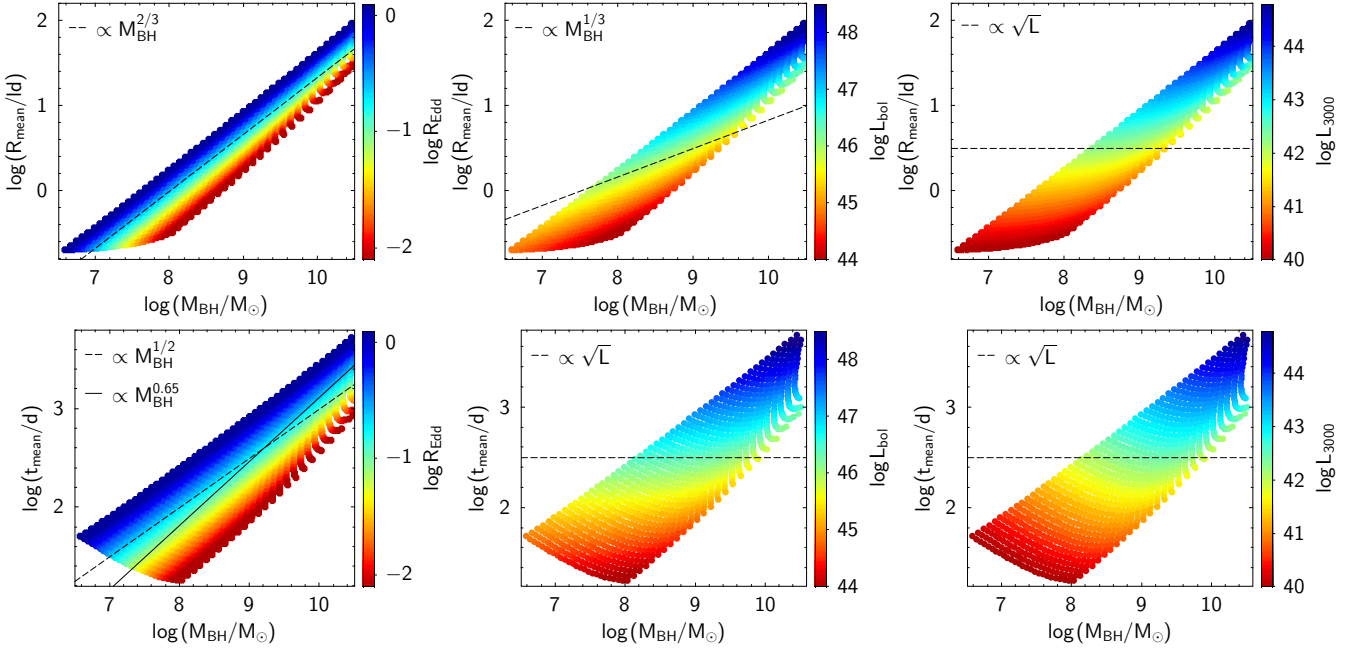


Figure 1. Flux-weighted size scale (mean emission radius) R_{mean} (top) and orbital time scale t_{mean} (bottom) at $\lambda = 3000 \text{ \AA}$ for a range of accretion discs (GR approximation with spin $a = 0$) using three colour codes: Eddington ratio R_{Edd} (left), true bolometric luminosity L_{bol} (centre), and monochromatic luminosity L_{3000} (right), which often acts as a proxy for L_{bol} . Dashed lines show the scaling by Morgan et al. (2010), and the solid line is from Arévalo et al. (2024).

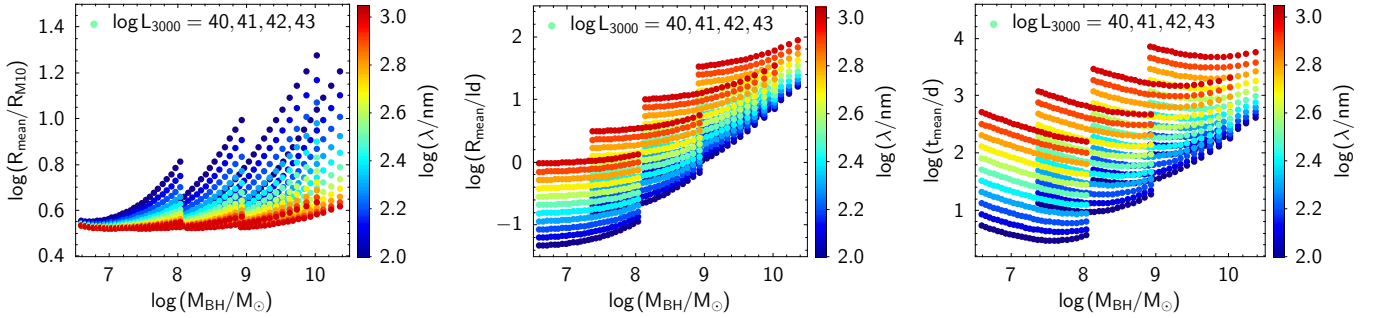


Figure 2. Left: Ratio of flux-weighted size scale (mean emission radius) R_{mean} to analytic size approximation in Morgan et al. (2010), R_{M10} , colour-coded by emission wavelength λ (GR approximation with spin $a = 0$). For optical wavelengths, the flux-weighted sizes are $\sim 5\times$ larger than R_{M10} , but the scales of UV emission may be enlarged by the large R_{ISCO} around the most massive black holes. Four groups of accretion discs are shown, with $\log L_{3000}/(\text{erg s}^{-1} \text{ \AA}^{-1})$ values of 40, 41, 42 and 43; their black-hole masses range according to the Eddington ratio limits of the calculated grid. Centre: Flux-weighted size scale R_{mean} vs. black-hole mass of the same discs. Right: Flux-weighted orbital time scale t_{mean} vs. black-hole mass of the same discs.

masses. The mass-independent scaling from Morgan et al. (2010) will capture the average scales across the turnaround at intermediate masses of $\log M_{\text{BH}} \sim 9$, with modest residuals. However, the size scale defined by Morgan et al. (2010), which is

$$R_{\text{M10}} = \left(\frac{45G\lambda_{\text{rest}}^4 M_{\text{BH}} \dot{M}}{16\pi^6 h_{\text{p}} c^2} \right)^{\frac{1}{3}} \quad (14)$$

$$= 9.7 \times 10^{15} \left(\frac{\lambda_{\text{rest}}}{\mu\text{m}} \right)^{\frac{4}{3}} \left(\frac{M_{\text{BH}}}{10^9 M_{\odot}} \right)^{\frac{2}{3}} \left(\frac{L_{\text{bol}}}{\eta L_{\text{Edd}}} \right)^{\frac{1}{3}} \text{cm},$$

where G is the gravitational constant, \dot{M} the accretion rate, and $\eta = L_{\text{bol}}/(\dot{M}c^2)$ is the radiative efficiency (0.057 for spin $a = 0$), typically underestimates the flux-weighted emission radius by a factor of 3 to 4 for visual light, and more for UV light from discs around very massive black holes (see Fig. 2, left panel).

3.2 Scaling at fixed luminosity and wavelength dependence

As stated, we consider the observable with the lowest uncertainty to be a monochromatic luminosity (ideally from a spectrum fit) such as L_{3000} , followed by black-hole mass M_{BH} in second place. The Eddington ratio R_{Edd} comes last in this list, as it combines errors from the two previous observables and includes mass-dependent biases in the bolometric correction. Hence, we now consider the disc scaling behaviour with black-hole mass at fixed observed L_{3000} .

In Figure 2 we show again the mass dependence of the size and orbital time scales, but this time for just a few choices of observed luminosity L_{3000} and instead several steps in wavelength. At low black-hole mass and thus small R_{ISCO} , a change in mass has little effect on the extent and appearance of the disc and thus its size scale (centre panel). But at intermediate masses, an increasing $R_{\text{ISCO}} \propto M$

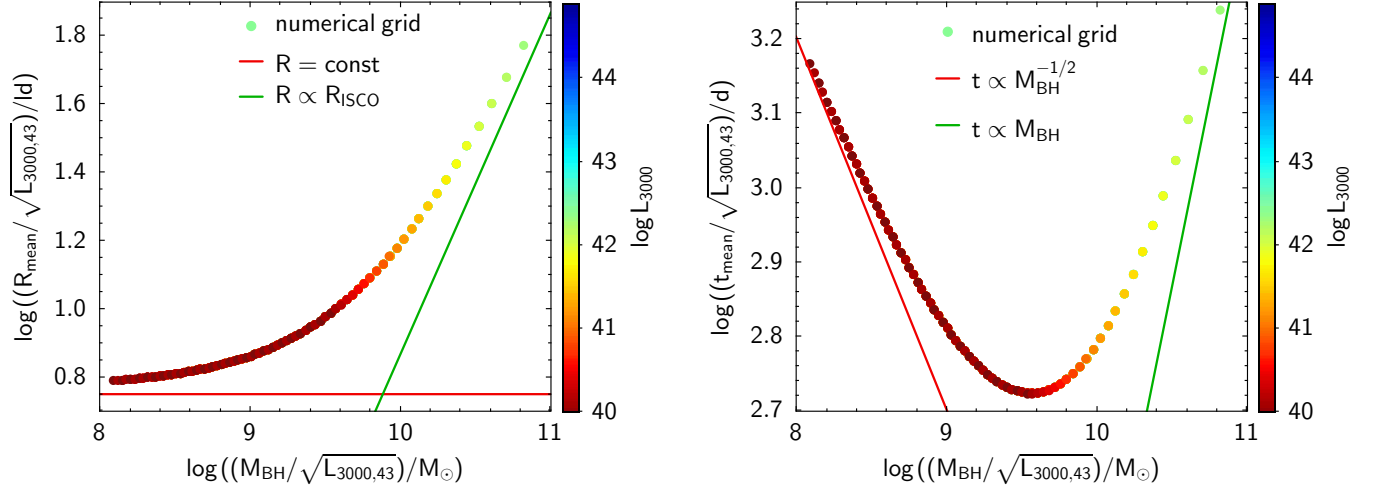


Figure 3. Luminosity-scaled size scales (left) and time scales (right) vs. luminosity-scaled black-hole mass at emission wavelength $\lambda = 3000 \text{ \AA}$ for a range of accretion discs (GR approximation with spin $a = 0$). For brevity, we use $L_{3000,43} = L_{3000}/(10^{43} \text{ erg s}^{-1} \text{ \AA}^{-1})$. A warped 2D surface is seen in projection as a 1D line. Every point in this figure represents a 1-parameter family of discs with different L_{3000} but identical $R_{\text{mean}}/\sqrt{L_{3000}}$ and identical $t_{\text{mean}}/\sqrt{L_{3000}}$. The variation of points seen in the projected plane is caused by variations in $R_{\text{ISCO}}/R_{\text{mean}}$.

moves the inner disc edge outwards, pushing it against the small-mass R_{mean} and eventually driving R_{mean} out at a rate that will approximate $R_{\text{mean}} \propto R_{\text{ISCO}} \propto M$. For the orbital time scales (right panel), we then find at low masses, where size scales are nearly constant, that the orbital velocity changes as $v \propto M^{1/2}$ and thus the time scale declines with increasing mass as $t_{\text{orb}} \propto R/v \propto M^{-1/2}$. At large masses, in contrast, the rapidly increasing size scale affects the orbital time scales more strongly than the declining orbital periods at fixed radius, causing $t_{\text{orb}} \propto R/v \propto (R^3/M)^{1/2} \propto M$. Between these two convergence regimes, the orbital timescale reaches a minimum at a mass that depends on luminosity and wavelength (see Figure 2). At $\lambda = 3000 \text{ \AA}$ and $\log L_{\text{bol}}/(\text{erg s}^{-1}) = 47$, the minimum time scale is reached at $\log M_{\text{BH}} \approx 9.5$.

3.3 Reconsidering the 2-parameter family

We now investigate further how $M_{\text{BH},\text{tmin}}$ depends on luminosity and wavelength. The simple model of a 1-parameter family scaled by size predicts a constant mean surface luminosity for a fixed temperature profile with inner and outer edges that scale in tune with the overall disc. In this case, we expect R_{mean}/\sqrt{L} to be invariant, and at a fixed mass t_{mean}/\sqrt{L} as well. The outer disc edge can be defined as a fixed temperature point, which will scale in tune with the overall disc scale given the temperature point asymptotes to a common power law in temperature for all discs. The inner disc edge depends on black-hole mass, so we can choose a pivotal mass as the one that keeps the inner edge scaling with the overall disc scale as well. Ignoring the effect of black-hole spin for now, $R_{\text{ISCO}} \propto M_{\text{BH}}$, so that the pivotal mass could be chosen as M_{BH}/\sqrt{L} .

Thus, the 2-parameter family of discs spanned by an overall size scale and an inner-edge scale should appear as a 1-parameter family of R_{mean}/\sqrt{L} as a function of M_{BH}/\sqrt{L} . This effect is confirmed by Figure 3, where R_{mean}/\sqrt{L} and t_{mean}/\sqrt{L} is shown for a single emission wavelength but for discs of all masses and luminosities, which form a curved surface seen in an ideal 1-D projection, where not all points are visible because the symbols are opaque and hiding points from the gridded surface in the background. At lowest and highest black-hole masses the scales approach the two analytically

expected limiting behaviours. At low black-hole masses, the spatial appearance of the discs is independent of the ISCO and the black-hole mass, while the orbital time scale declines with $M_{\text{BH}}^{-1/2}$; at high black-hole masses, the spatial appearance of the discs will be driven by the ISCO and thus black-hole mass, such that the size scales will increase as $R_{\text{mean}} \propto R_{\text{ISCO}} \propto M_{\text{BH}}$ and the orbital time scales with $t_{\text{mean}} \propto R_{\text{ISCO}}^{3/2} M_{\text{BH}}^{-1/2} \propto M_{\text{BH}}$. The dependence on wavelength should follow the temperature profile with $R_{\text{mean}} \propto \lambda^{4/3}$ and $t_{\text{mean}} \propto R_{\text{mean}}^{3/2} \propto \lambda^2$ at least in the low-mass regime.

In the following section, we develop an analytic approximation to the numerically calculated surface by using a smoothly broken power law incorporating the outlined, expected power law characteristics.

4 A NEW APPROXIMATION

We wish to assist future evaluations of size and time scales in simple thin-disc models by deriving an analytic approximation of $R_{\text{mean}} = f(L_{3000}, M_{\text{BH}}, \lambda)$ and $t_{\text{mean}} = f(L_{3000}, M_{\text{BH}}, \lambda)$ for different innermost stable orbits of $R_{\text{ISCO}}/R_{\text{S}} = (1.5, 3, 4.5)$ corresponding to black-hole spins of $a = (+0.78, 0, -1)$. These will not be single power laws but smoothly broken power laws that approximate the numerical calculations while morphing from typical low-mass scaling, where scales are independent of the ISCO, to typical high-mass scaling, where scales are driven by the ISCO. For brevity, we will use the notation $L_{3000,43} = L_{3000}/(10^{43} \text{ erg s}^{-1} \text{ \AA}^{-1})$.

We use the general approach of smoothly broken power laws

$$y = y_0 \times \left[\left(\left(\frac{x}{x_1} \right)^{s_1} \right)^\gamma + \left(\left(\frac{x}{x_2} \right)^{s_2} \right)^\gamma \right]^{1/\gamma},$$

where $x = M_{\text{BH}}/\sqrt{L_{3000,43}}$, the size scale is $y_r = R_{\text{mean}}/\sqrt{L_{3000,43}}$ and the time scale is $y_t = t_{\text{mean}}/\sqrt{L_{3000,43}}$ at fixed wavelength λ_{rest} and black-hole spin a . After applying expected scaling behaviour and factoring in a reference wavelength λ_0 (in units of \AA), we get

$$y_r = \left[\left(C_r \left(\frac{\lambda}{\lambda_0} \right)^{4/3} \right)^{\gamma_r} + \left(\frac{x}{x_{\text{br},r}(\lambda)} \right)^{\gamma_r} \right]^{1/\gamma_r}, \text{ and} \quad (15)$$

$$y_t = \left[\left(\left(\frac{\lambda}{\lambda_0} \right)^2 \left(\frac{x}{x_0} \right)^{-1/2} \right)^{\gamma_t} + \left(\frac{x}{x_{\text{br},t}(\lambda)} \right)^{\gamma_r} \right]^{1/\gamma_t}. \quad (16)$$

After inspecting first results, we choose a further broken power-law parametrisation for the λ -dependence of $x_{\text{br},r}$ and proportionalities between size and time scale parameters. Our best-fit solution then is:

$$\lambda_0 \equiv 3000 \text{ \AA}, C_r \approx 5.896, x_0 \approx 2.279 \times 10^{14}, \quad (17)$$

$$x_{\text{br},r}(\lambda, \hat{a}) = \left[\zeta(\hat{a})^{\gamma_{\text{br}}} + \left(\frac{\lambda}{\zeta(\hat{a})\lambda_{\text{br}}} \right)^{-\gamma_{\text{br}}} \right]^{1/\gamma_{\text{br}}}, \quad (18)$$

$$\log(\zeta(\hat{a})) = 9.29 + 0.15\hat{a}, \log \lambda_{\text{br}} = 3.66, \gamma_{\text{br}} = -1.437, \quad (19)$$

$$\log x_{\text{br},t} = \frac{3}{2}(\log x_{\text{br},r} - 4), \quad (20)$$

$$\frac{3}{2}\gamma_t(\lambda) = \gamma_r(\lambda) = C_0 + C_1 \log \lambda, \quad (21)$$

$$C_0 = 1.683, C_1 = -0.246, \hat{a} = (6 - 2R_{\text{ISCO}}/R_S)/3. \quad (22)$$

This parametric solution agrees with the numerical calculations to < 0.01 dex for most of the grid range in both $\log R_{\text{mean}}$ and $\log t_{\text{mean}}$; however, at large masses and small luminosities, the deviation can reach 0.05 dex; Figure 4 shows the quality and residuals of the fit.

5 HIGH BLACK-HOLE MASS QSOS

In this section, we study light curve variability in a sample of quasars that we believe has a good chance to take us away from the low-mass scaling behaviour and probe the turnover regime in the disc timescales. Such a test could help to reveal whether the variability of quasar discs is indeed driven by the disc timescales or merely shows some not-yet understood scaling with disc and black hole properties.

5.1 Data and sample

We use the same quasar sample and light curve data that have been used in previous studies of the variability structure function by Tang et al. (2023) and Tang et al. (2024). The sample started with the $\sim 5,000$ brightest radio-quiet quasars in the sky at $\delta > -45^\circ$, i.e., in the $> 3\pi$ srad region of sky that has been monitored by the NASA Asteroid Terrestrial-impact Last Alert System (ATLAS, Tonry et al. 2018) for several years already. Following Tang et al. (2024), we restrict the sample to those which have virial single-epoch estimates of black-hole mass and estimates of 3000\AA continuum luminosity from spectral decomposition presented in the catalogue by Rakshit et al. (2020). We focus on the orange passband (ρ -band) which dominates the ATLAS data with the best cadence due to its continuous imaging throughout the lunar cycle.

The aim is to correct the variability of quasars for trends with wavelength and trends with luminosity so that any dependence on the black-hole mass can be isolated. We thus avoid redshifts, where the orange passband probes regions of the quasar spectrum that are not easy to correct for passband shifting. At $z \lesssim 1$ the orange passband probes a part of the disc emission that does not follow the simple wavelength relation of $\log A \propto -\log \lambda$ present at $\lambda_{\text{rest}} < 3500 \text{ \AA}$ but instead flattens towards longer wavelengths as shown by Tang et al. (2023) and earlier observed by Caplar et al. (2017). For convenience and consistency with past binning and calculations, we choose a cutoff of $z > 0.96$. Since the flattening is not well characterised at this stage, it is difficult to correct for the purpose of bringing quasars from all redshifts onto a common wavelength-independent scale. We

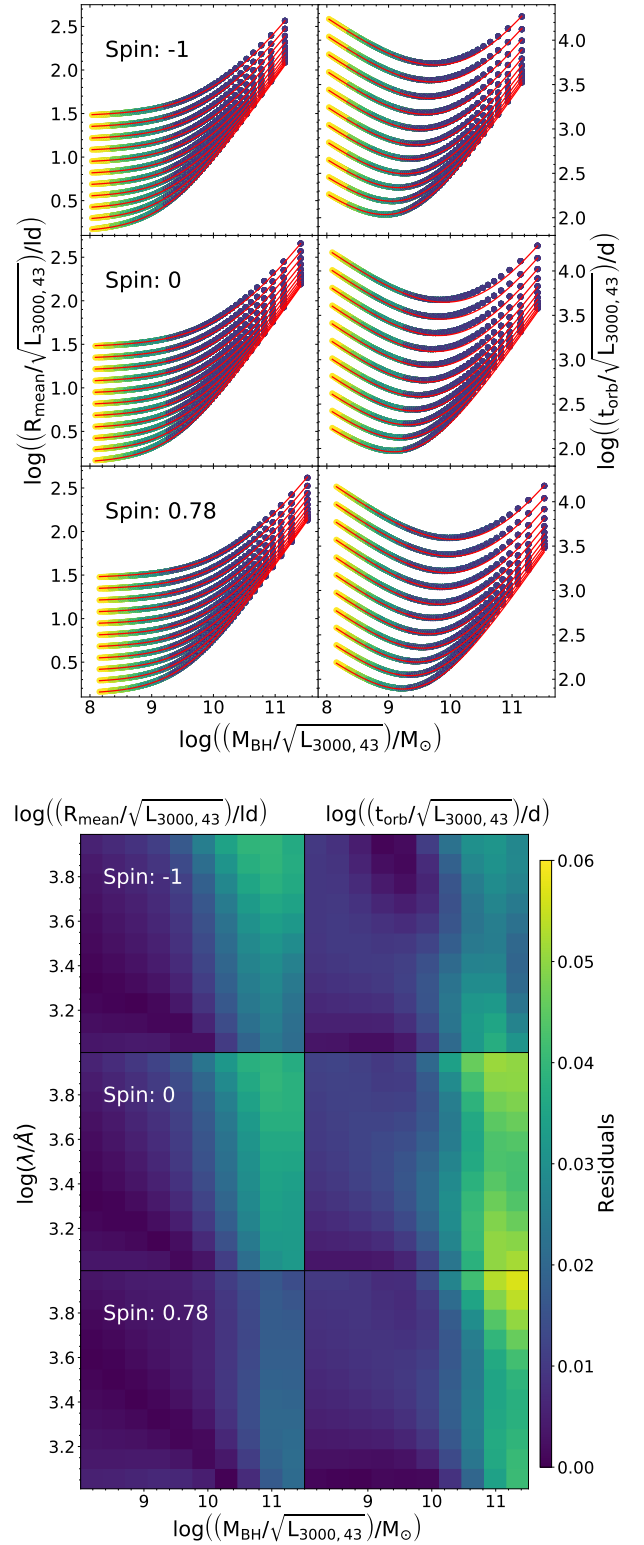


Figure 4. Illustration of the analytic approximation to size and time scales in simple thin-disc models. *Top:* Grid points are displayed as points and the analytic fits are plotted as lines. The colour scale represents the range of Eddington ratios and lines in a single panel are differentiated by wavelength. *Bottom:* Residuals as a function of wavelength and mass, showing that while the analytic solution is typically within 0.01 dex of the numerical calculation, the deviation can reach 0.05 dex at high masses and low luminosities.

also exclude quasars at $z > 2.4$, where the important L_{3000} luminosity is not probed by the spectral fitting in Rakshit et al. (2020), but would require risky extrapolation instead, and furthermore the data become sparse and the structure functions noisy. This selection leaves us with 2,189 quasars, with a median luminosity of $\log L_{3000} = 42.9$ (or $\log L_{\text{bol}} \approx 47$ using standard estimates) and a median black-hole mass of $\log M_{\text{BH}} = 9.35$. The median redshift of $z \approx 1.6$ implies that the median rest-frame wavelength probed by the ATLAS o -band is $\lambda_{\text{rest}} = 2600 \text{ \AA}$. The Rakshit et al. (2020) luminosities assume a flat Λ CDM cosmology with $\Omega_{\Lambda} = 0.7$ and $H_0 = 70 \text{ km s}^{-1} \text{ Mpc}^{-1}$.

Following Tang et al. (2023) and Tang et al. (2024), we also apply identical cleaning steps to the light curve data to reject outliers, and we apply the improved noise model by Tang et al. (2024) to avoid biasing the structure function around the less well-defined, weaker variability on short time scales. On average, light curves have more than 1900 photometric points over 7 years of data from 30 May 2017 to Aug/Sep 2024 (varying from object to object). We split the sample into four redshift bins with ~ 547 objects each and further into bins with near-equal object numbers in luminosity and mass, using 5×5 bins in $L_{3000} \times M_{\text{BH}}$ with ~ 22 objects on average. We determine the ensemble structure function for each bin from an average of ~ 30 million magnitude pairs combined over ~ 22 objects.

5.2 Variability structure function

As in Tang et al. (2024), we adopt the noise-corrected definition of variability amplitude from Di Clemente et al. (1996):

$$A = \sqrt{\frac{\pi}{2} < \Delta m >^2 - < \sigma^2 >}, \quad \text{with } \Delta m = |m_i - m_j|, \quad (23)$$

where m_i and m_j are any two observed apparent magnitudes and σ is the magnitude error due to noise. The mean error $< \sigma^2 >$ is taken to be revealed by the measured level of intra-day variability ($\Delta t < 1 \text{ d}$), which is assumed to be intrinsically close to zero and thus forced to $A = 0$. This approach has been suggested by Kozłowski (2016) and is plausible as the typical amplitude of intra-day variability in radio-quiet quasars is much smaller than our noise level and will not noticeably affect the analysis of the random walk portion in the SF. Furthermore, Tang et al. (2024) have shown that on our data set this approach is superior than a magnitude-dependent approximation of the noise attempted previously in Tang et al. (2023).

We evaluate the structure function in bins of rest-frame time intervals Δt_{rest} up to $\log \Delta t_{\text{rest}} = 2.4$. We do not consider magnitude pairs with longer time separation as these might be affected by window effects from the finite length of the light curves. As in Tang et al. (2024), we then fit linear functions to the binned structure function using a random-walk slope of $1/2$ as deemed appropriate by Tang et al. (2023) for this high-luminosity data set. We use only data from the window $\log \Delta t_{\text{rest}} = [1.4; 2.4]$, as at shorter Δt various authors have claimed to see a steepening in the slope of certain AGN samples. While Tang et al. (2024) found no conclusive evidence of such steepening, we avoid the regime at $\log \Delta t_{\text{rest}} < 1.4$ to avoid any possible biases from a subtle steepening. Thus, the only free parameter of the fit is the intercept $\log A_{1.9}$, which is the structure function amplitude at the midpoint in the fit interval, $\log(\Delta t_{\text{rest}}/\text{d}) = 1.9$ (or ~ 80 days), as part of the form $\log A = \log A_{1.9} + 1/2 \times (\log \Delta t_{\text{rest}} - 1.9)$. The $A_{1.9}$ can then be plotted against wavelength, luminosity, and mass.

We note, that studies of lower-luminosity QSOs fit breaks in structure functions and aim to measure their time scales (e.g., Arévalo et al. 2024); but as evident in Tang et al. (2024), we do not see any breaks in our data, which might be a consequence of long intrinsic disc time scales for objects as extreme as those studied here.

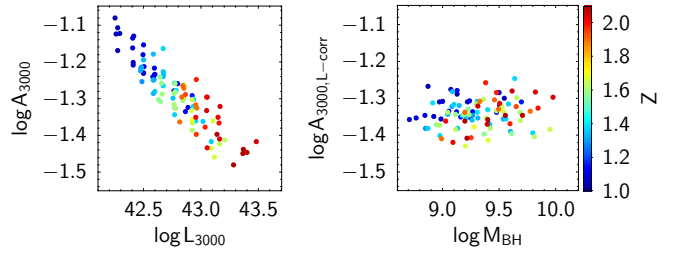


Figure 5. Intercept of the variability structure function fit at $\log \Delta t_{\text{rest}} = 1.9$, normalised to a wavelength of $\lambda_{\text{rest}} = 3000 \text{ \AA}$. *Left:* Intercept vs. continuum luminosity at 3000 \AA ; a well-known dependence on luminosity is evident. *Right:* intercept vs black-hole mass estimate after subtracting the luminosity dependence, showing little residual mass dependence.

5.3 Results

From the results of the structure function fitting, we confirm that the intercept follows the relationship $\log A_{1.9} \propto -\log \lambda - 1/4 \log L_{3000}$ as determined previously by Tang et al. (2023) from a larger sample of quasars that contains the sample and light curves used here; the sample used here is restricted to objects with known black-hole masses and well-constrained L_{3000} measurements in a restricted redshift range. Figure 5 shows the intercepts after correcting for the wavelength dependence in the structure function (with colour-coding by redshift) and transforming from the observed frame wavelength of $\lambda_{\text{pivot}} = 6750 \text{ \AA}$ to the restframe wavelength of 3000 \AA , using $\log A_{3000} = \log A_{1.9} - \log(1+z) \times (3.0/6.75)$, plotted vs. L_{3000} in the left panel; the previously measured slope of $-1/4$ is clearly evident. After correcting the intercepts further for this luminosity dependence using $\log A_{3000, \text{L-corr}} = \log A_{3000} + 1/4 \times (\log L_{3000} - 43)$, the right panel shows the corrected intercepts as a function of black-hole mass in search of remaining trends; the results is consistent with no black-hole mass dependence within the errors, as assumed by the Morgan et al. (2010) approximation used also by Tang et al. (2023).

Using the numerical disc calculations from this work, and assuming that the Tang et al. (2023) claim of a universal structure function of the form $\log A/A_0 = 1/2 \times \log \Delta t/t_{\text{mean}}$ holds, we expect at low black-hole masses $t_{\text{mean}} \propto M_{\text{BH}}^{-1/2}$ and thus $\log A/A_0 = 1/2 \times \log \Delta t + 1/4 \times \log M_{\text{BH}} + c_1$; at higher masses, we expect a transition point without mass dependence ($t_{\text{mean}} = \text{const}$) such that $\log A/A_0 = 1/2 \times \log \Delta t + c_2$; and finally, at the highest masses we expect to converge into the form $t_{\text{mean}} \propto M_{\text{BH}}$ and thus $\log A/A_0 = 1/2 \times \log \Delta t - 1/2 \times \log M_{\text{BH}} + c_3$.

For a closer comparison with the model prediction derived in Section 3, we zoom into the relevant mass range of the right panel of Figure 3 and overplot the data from our structure functions (see Figure 6). However, we do not know a-priori what level of amplitude $\log A$ to expect for $\Delta t = t_{\text{mean}}$, and first aim to normalise the expected structure function amplitude. The spin-free model grid specifies the orbital timescale to be $\log(t_{\text{mean}}/\text{d}) = 2.71$ (or $t_{\text{mean}} = 513$ days) for $(\log M_{\text{BH}}, \log L_{3000}, \lambda_{\text{rest}}/\text{\AA}) = (9.5, 43.0, 3000)$. At these physical parameters, our data show on average $\log A = -1.33$ at $\log \Delta t/\text{d} = 1.9$. Thus, the best fit of the model-predicted orbital timescales to our data in the form $\log A/A_0 = -1/2 \times \log \Delta t/t_{\text{mean}}$ yields $\log A_0 = -0.925$ (the value of A_0 determined in Tang et al. (2023) is different as it refers to the thermal timescale instead of the orbital timescale and it uses a normalisation derived from Morgan et al. (2010)). For each sample bin, we now transform the fitted intercept $\log A_{1.9}$ into an SF-estimated mean orbital timescale using

$$\log t_{\text{mean}} = -1/\gamma (\log A_{1.9} - \log A_0) + 1.9 = -2 \log A_{1.9} + 0.05, \quad (24)$$

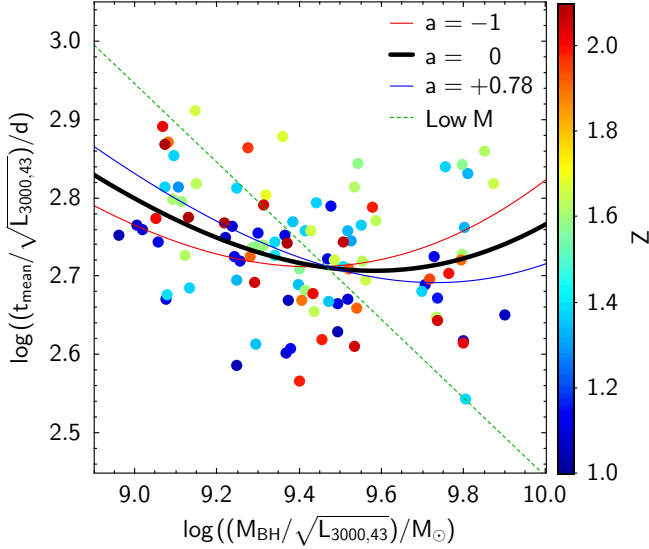


Figure 6. Comparison of orbital timescales as derived from the amplitude normalisation of structure function data and the approximation from Sect. 4 for different black-hole spins (solid lines). The plot zooms into the right panel of Figure 3. The small-hole approximation with a slope of $-1/2$ (dashed line) is ruled out and fares worse than mass independence. However, the data are also consistent with the shape of the predicted turnover in the spin-free model or models with $a > 0$, with an RMS scatter around of ~ 0.07 dex. The location $M_{\text{BH}}/\sqrt{L_{3000}}$ of the minimum in $t_{\text{mean}}/\sqrt{L_{3000}}$ will shift, however, not only with black-hole spin, but also with biases in luminosity measurements from, e.g., host galaxy dust extinction, restricted inclination in quasar samples, and any deviations of real discs from the idealised thin discs modelled here.

and then plot $y = \log(t_{\text{mean}}/\sqrt{L_{3000,43}})$ vs. $x = (M_{\text{BH}}/\sqrt{L_{3000,43}})$ in Figure 6. The approximation $y(x)$ from Sect. 4 is overplotted for three different values of the black-hole spin. While the agreement in the mean level of y has been engineered by fitting the normalisation A_0 to our data, we focus on comparing the trend of y with x : we still see that the y values are nearly independent of black-hole mass, and are certainly incompatible with a $-1/2$ slope predicted for lower masses. The data also seem to follow the predicted line for spin-free black holes or those with modest prograde spins within the errors. The scatter in the data is too large to distinguish with high confidence between the predicted turnover and no black-hole mass dependence at all. However, given that structure functions for accretion discs around lower-mass black holes have shown a decline of characteristic timescales with increasing mass (e.g. Arévalo et al. 2024), even the observation of a flat mass dependence in the regime of our sample validates the basic turnover geometry proposed here.

6 DISCUSSION

The agreement demonstrated between our structure function data and the emission-weighted disc timescales derived from the simple thin accretion disc model in this paper whets an appetite for more precise data. It appears that a measurement of the turnover location in $M_{\text{BH}}/\sqrt{L_{3000}}$ might constrain, e.g. average black-hole spins in a sample. However, we note several limitations here: (1) The measured luminosity is affected by anisotropic disc emission, and thus changing the mix of inclination angles in a sample of accretion discs will shift the x-axis of the prediction. (2) The luminosity may also be affected

by mild extinction from host galaxy or nuclear dust, which would again shift the x-axis. Thus, black-hole spin, disc inclination, and dust extinction are degenerate in this diagnostic.

The catalogue values of L_{3000} are derived without any inclination correction and thus overestimate the luminosity for viewing angles close to face-on. For an angle of $i = 30^\circ$ between the spin axis and the line-of-sight, e.g., we overestimate L_{3000} relative to the true total disc emission by ~ 0.24 dex (see appendix of Lai et al. 2023). This means that the data points in Figure 6 would need to be shifted 0.12 dex to the right and up. This shift would be countered by dust extinction and indeed by neutralised exactly in the case of $A_{3000} = 0.6$ mag, which corresponds to a reddening of $E(B - V) \approx 0.12$ assuming the dust extinction law with $A_{3000}/A_V = 1.86$ from Gallerani et al. (2010) and a Small Magellanic Cloud-like $R_V = 2.7$ (Bouchet et al. 1985); or, for the flatter Calzetti et al. (1994) extinction law, the $E(B - V)$ reddening needed to achieve a similar extinction would be smaller. Note, that any upwards shift is irrelevant as it would also affect A_0 and equation 24 and thus cancel out in the model comparison.

We also point out, that the measured amplitude of the brightness variations underestimates the true variability of the disc continuum because the total object flux in the observing passband includes contributions from broad emission lines and Balmer continuum. On average, the fraction of L_{3000} from the accretion disc is $\sim 80\%$, and while the variability of the emission lines is driven by that of the disc, the light curves are out of phase due to light travel time. If, to first order, the simultaneous emission-line variability is not correlated with the disc variability, then the fractional variability signal in the total light curve of the objects will be underestimated by this factor; on average this would increase $\log A_0$ by ~ 0.1 dex but with some dependence on redshift and spectral properties of the quasar.

At a more technical level we note, that the formal fit errors for the intercept of the structure functions (~ 0.02 dex) are smaller than the scatter of intercepts (~ 0.07 dex) seen among the different sample bins. However, the fit errors may be understated compared to the true uncertainty of the determined intercept because the amplitude values of the structure function for different bins in time separation are not statistically independent. A more elaborate determination of more realistic errors would involve bootstrapping, which is beyond the scope of the analysis presented here.

Further to that, we expect biases when comparing bins of different disc luminosity at a fixed redshift: torus opening angles set the range and mix of inclination angles in a sample of type-1 AGN; if these depend on disc luminosity, then we expect mean luminosity biases from the anisotropic disc emission that change with luminosity itself; even in the absence of intrinsic trends of opening angle, intermediate luminosity bins may contain a standard distribution of inclination angles, while the highest-luminosity tail of the distribution at any redshift would be dominated by accretion discs viewed face-on and thus tend to overestimate the mean luminosity in the bin relative to the lower- L bins. Similarly, if modest dust extinction plays a role in the average quasar, the highest-luminosity tail of the distribution would be dominated by the lowest-extinction objects.

Correcting the aforementioned effects as best as possible is beyond the scope of this paper, and may require forward modelling while testing a range of alternative assumptions. If future data sets with higher precision are combined with potential diagnostics of inclination and dust, perhaps in the form of spectral energy distributions and emission-line ratios and profiles, they might reveal trends and inconsistencies with the simple model at higher fidelity than what has been attempted here.

7 CONCLUSIONS

There are literature studies of how UV-optical variability in AGN depends on their black-hole mass (including most recently [Arévalo et al. 2024](#)), although some works ignore this dependence (including [Tang et al. 2023](#)). A specific dependence considered since [Balbus & Hawley \(1991\)](#) and [Kelly et al. \(2009\)](#) is that variability behaviour may depend on orbital or thermal timescales of the emitting accretion disc. The question then becomes how these depend on black-hole mass and whether that matches observed trends. In this paper, we have revealed how both approaches, ignoring black-hole mass or specifically controlling for it, can be valid, depending on the part of AGN parameter space that is considered.

We first model standard thin accretion discs and evaluate orbital timescales of the disc over the following parameter ranges: the rest-frame wavelength of disc emission, $\log(\lambda_{\text{rest}}/\text{\AA}) = [3; 4]$, the black-hole mass, $\log(M_{\text{BH}}/M_{\odot}) = [6; 11]$, the Eddington ratio of the disc, $\log(R_{\text{Edd}}) = [-2; 0]$, and black-hole spin values of $a = (+0.78, 0, -1)$. Before studying dependencies, we calculate the monochromatic 3000Å disc luminosity, L_{3000} , which is a more robustly determined observable than R_{Edd} .

As a result, we find two regimes in the timescale dependence on black-hole mass, with a turnover in between: at low masses, we see the decline of $t_{\text{orb}} \propto M^{-1/2}$, which is a textbook expectation of orbits speeding up with increasing central mass. Towards extremely massive black holes, we observe that a growing event horizon and innermost stable circular orbit (ISCO) around the black hole push the emission region farther from the black hole such that we see an increase in timescale with mass, $t_{\text{orb}} \propto M$. These two regimes are connected by a transition region, where the mass dependence vanishes locally. The relation between disc timescale and black-hole mass is thus not a simple power law but a smoothly broken power law. For the benefit of the reader, we approximate the numerical grid model with convenience functions that express the mean emission radius and the mean orbital timescale as a function of wavelength, black hole mass, monochromatic luminosity, and black-hole spin.

It might come as a surprise to intuition that the transition regime, let alone the rising branch, of timescales matters in the parameter space of observed quasar samples. In fact, the black-hole mass that minimises disc time scales for a disc with $\log L_{\text{bol}}/(\text{erg s}^{-1}) = 47$ is $\log M_{\text{BH}} \approx 9.5$. We thus re-evaluate variability structure functions of the brightest ~ 200 quasars with virial black-hole mass estimates and L_{3000} continuum luminosity estimates from spectral fitting by [Rakshit et al. \(2020\)](#), using light curves from NASA/ATLAS ([Tonry et al. 2018](#)) in the well-sampled orange passband that span over 7 years in duration with nearly 2000 visits per object on average. This sample has an estimated median black-hole mass of $\log M_{\text{BH}} \approx 9.35$, an estimated median bolometric luminosity of $\log L_{\text{bol}}/(\text{erg s}^{-1}) \approx 47$, and a median redshift of $z \approx 1.6$, implying that the median rest-frame wavelength probed by the ATLAS o -band is $\lambda_{\text{rest}} = 2600 \text{\AA}$. As the sample is almost centred on the turnover regime in disc timescales predicted by our disc calculations, it is expected to exhibit little mass dependence. In hindsight, this provides justification to [Tang et al. \(2023\)](#), who chose to ignore a black-hole mass dependence in their estimates of disc timescales.

This is in relevant contrast to other observations of variability behaviour at lower black-hole masses that reveal a dependence on mass (e.g. [Arévalo et al. 2024](#)). The two behaviours combined might merely point at a non-trivial mass dependence in the disc variability. However, the remarkable fact is that both, observed mass dependence at lower mass in other works, and independence at the higher masses in this work, mimics the expectation from a simple thin-disc model,

where amplitude is fixed on timescales in units of mean timescale of the predicted disc emission. At a subtle level, the analysis presented here suggests that the quasar discs in this work follow the curvature of the predicted turnover in timescale, although both noise and currently unconstrained biases may have blurred the agreement.

The result of this paper is thus a strong suggestion that a simple thin disc model paired with a simple phenomenological expectation of variability as following $\log A/A_0 = -1/2 \times \Delta t/t_{\text{mean}}$ may robustly portray stochastic variability of quasar accretion discs, as suggested before by [Tang et al. \(2023\)](#). This situation promises opportunities to constrain physical disc parameters from an observation of the structure function, as the observed amplitude normalisation would encode black-hole mass, luminosity, black-hole spin, inclination, and dust extinction, although in degenerate form. With black-hole mass measured independently, and other disc properties considered nuisance parameters, there may be a chance to consider the structure function an independent diagnostic of true disc luminosity. It could be combined with other diagnostics that calibrate quasars as standard candles, to enhance their precision as tools for cosmology (e.g. [Risaliti & Lusso 2019](#)). Many diagnostics of quasar discs, such as spectral energy distribution (SED), profiles and flux ratios of strong emission lines, the X-ray-to-UV spectral index, α_{OX} (see e.g. [Liu et al. 2021](#)), appear to correlate with disc properties including orientation and Eddington ratio (e.g. [Shen & Ho 2014](#)), but are degenerate between several intrinsic parameters when used in isolation. By combining multiple diagnostics, and from now onwards, adding the structure function into the mix, it may be possible to break degeneracies and disentangle the parameters in observed objects.

This outlook motivates high-precision observations of UV-optical variability in many quasar discs, such as will be enabled by the Legacy Survey of Space and Time (LSST; [Ivezic et al. 2008](#)) soon to start at the new Vera C. Rubin Telescope (VRO) in Chile. However, for brighter quasars that saturate in LSST observations, NASA/ATLAS, the Zwicky Transient Facility (ZTF; [Bellm et al. 2019](#)) and others will continue to play an important role.

ACKNOWLEDGEMENTS

JJT was supported by the Taiwan Australian National University PhD scholarship and the Australian Research Council (ARC) through Discovery Project DP190100252 and also acknowledges support by the Institute of Astronomy and Astrophysics, Academia Sinica (ASIAA). JT was supported by the Stromlo Distinguished Visitor Program at RSAA. We thank Zachary Steyn for helping to remove ambiguities in the manuscript.

This research has made use of IDL. This work uses data from the University of Hawaii’s ATLAS project, funded through NASA grants NN12AR55G, 80NSSC18K0284, and 80NSSC18K1575, with contributions from the Queen’s University Belfast, STScI, the South African Astronomical Observatory, and the Millennium Institute of Astrophysics, Chile.

This work has made use of SDSS spectroscopic data. Funding for the Sloan Digital Sky Survey IV has been provided by the Alfred P. Sloan Foundation, the U.S. Department of Energy Office of Science, and the Participating Institutions. SDSS-IV acknowledges support and resources from the Center for High Performance Computing at the University of Utah. The SDSS website is <http://www.sdss.org>. SDSS-IV is managed by the Astrophysical Research Consortium for the Participating Institutions of the SDSS Collaboration including the Brazilian Participation Group, the Carnegie Institution for Science, Carnegie Mellon University, Center for Astrophysics | Harvard &

Smithsonian, the Chilean Participation Group, the French Participation Group, Instituto de Astrofísica de Canarias, The Johns Hopkins University, Kavli Institute for the Physics and Mathematics of the Universe (IPMU) / University of Tokyo, the Korean Participation Group, Lawrence Berkeley National Laboratory, Leibniz Institut für Astrophysik Potsdam (AIP), Max-Planck-Institut für Astronomie (MPIA Heidelberg), Max-Planck-Institut für Astrophysik (MPA Garching), Max-Planck-Institut für Extraterrestrische Physik (MPE), National Astronomical Observatories of China, New Mexico State University, New York University, University of Notre Dame, Observatório Nacional / MCTI, The Ohio State University, Pennsylvania State University, Shanghai Astronomical Observatory, United Kingdom Participation Group, Universidad Nacional Autónoma de México, University of Arizona, University of Colorado Boulder, University of Oxford, University of Portsmouth, University of Utah, University of Virginia, University of Washington, University of Wisconsin, Vanderbilt University, and Yale University.

This work has made use of data from the European Space Agency (ESA) mission Gaia (<https://www.cosmos.esa.int/gaia>), processed by the Gaia Data Processing and Analysis Consortium (DPAC, <https://www.cosmos.esa.int/web/gaia/dpac/consortium>). Funding for the DPAC has been provided by national institutions, in particular the institutions participating in the Gaia Multilateral Agreement.

DATA AVAILABILITY

The data underlying this article will be shared on reasonable request to the corresponding author.

APPENDIX

Figure 7 shows a 3D view of the disc time scale in the luminosity-mass plane as calculated in the numerical grid.

REFERENCES

- Arévalo P., Churazov E., Lira P., Sánchez-Sáez P., Bernal S., Hernández-García L., López-Navas E., Patel P., 2024, *A&A*, **684**, A133
- Balbus S. A., Hawley J. F., 1991, *ApJ*, **376**, 214
- Bellm E. C., et al., 2019, *PASP*, **131**, 018002
- Bennett V. N., et al., 2021, *ApJ*, **921**, 36
- Bouchet P., Lequeux J., Maurice E., Prevot L., Prevot-Burnichon M. L., 1985, *A&A*, **149**, 330
- Burke C. J., et al., 2021, *Science*, **373**, 789
- Cackett E. M., Horne K., Winkler H., 2007, *MNRAS*, **380**, 669
- Calderone G., Ghisellini G., Colpi M., Dotti M., 2013, *MNRAS*, **431**, 210
- Calzetti D., Kinney A. L., Storchi-Bergmann T., 1994, *ApJ*, **429**, 582
- Campitiello S., Ghisellini G., Sbarrato T., Calderone G., 2018, *A&A*, **612**, A59
- Caplar N., Lilly S. J., Trakhtenbrot B., 2017, *ApJ*, **834**, 111
- di Clemente A., Giallongo E., Natali G., Trevese D., Vagnetti F., 1996, *ApJ*, **463**, 466
- Dalla Bontà E., et al., 2020, *ApJ*, **903**, 112
- Edelson R., Nandra K., 1999, *ApJ*, **514**, 682
- Frank J., King A., Raine D. J., 2002, *Accretion Power in Astrophysics: Third Edition*. <https://ui.adsabs.harvard.edu/abs/2002apa...book....F>
- Gallerani S., et al., 2010, *A&A*, **523**, A85
- Hanawa T., 1989, *ApJ*, **341**, 948
- Homayouni Y., et al., 2019, *ApJ*, **880**, 126
- Ivezic Z., et al., 2008, *Serbian Astronomical Journal*, **176**, 1
- Jiang Y.-F., Blaes O., 2020, *ApJ*, **900**, 25
- Jiang Y.-F., et al., 2017, *ApJ*, **836**, 186
- Kelly B. C., Bechtold J., Siemiginowska A., 2009, *ApJ*, **698**, 895
- Kelly B. C., Treu T., Malkan M., Pancoast A., Woo J.-H., 2013, *ApJ*, **779**, 187
- Kozłowski S., 2016, *ApJ*, **826**, 118
- Lai S., Wolf C., Onken C. A., Bian F., 2023, *MNRAS*, **521**, 3682
- Laor A., 1990, *MNRAS*, **246**, 369
- Laor A., Davis S. W., 2011, *MNRAS*, **417**, 681
- Lawrence A., 2016, in *Mickaelian A., Lawrence A., Magakian T., eds, Astronomical Society of the Pacific Conference Series Vol. 505, Astronomical Surveys and Big Data*. p. 107 ([arXiv:1605.09331](https://arxiv.org/abs/1605.09331)), [doi:10.48550/arXiv.1605.09331](https://doi.org/10.48550/arXiv.1605.09331)
- Lawrence A., Papadakis I., 1993, *ApJ*, **414**, L85
- Li L.-X., Zimmerman E. R., Narayan R., McClintock J. E., 2005, *ApJS*, **157**, 335
- Li Z., McGreer I. D., Wu X.-B., Fan X., Yang Q., 2018, *ApJ*, **861**, 6
- Liu H., Luo B., Brandt W. N., Brotherton M. S., Gallagher S. C., Ni Q., Shemmer O., Timlin J. D. I., 2021, *ApJ*, **910**, 103
- MacLeod C. L., et al., 2010, *ApJ*, **721**, 1014
- Malkan M. A., 1983, *ApJ*, **268**, 582
- Marziani P., et al., 2018, *Frontiers in Astronomy and Space Sciences*, **5**, 6
- McHardy I. M., Gunn K. F., Uttley P., Goad M. R., 2005, *MNRAS*, **359**, 1469
- Mejía-Restrepo J. E., Lira P., Netzer H., Trakhtenbrot B., Capellupo D. M., 2018, *Nature Astronomy*, **2**, 63
- Morgan C. W., Kochanek C. S., Morgan N. D., Falco E. E., 2010, *ApJ*, **712**, 1129
- Morganson E., et al., 2014, *ApJ*, **784**, 92
- Neustadt J. M. M., Kochanek C. S., 2022, *MNRAS*, **513**, 1046
- Novikov I. D., Thorne K. S., 1973, in *Black Holes (Les Astres Occlus)*. pp 343–450
- Palanque-Delabrouille N., et al., 2011, *A&A*, **530**, A122
- Paolillo M., et al., 2023, *A&A*, **673**, A68
- Peterson B. M., 2001, in *Aretxaga I., Kunth D., Mújica R., eds, Advanced Lectures on the Starburst-AGN*. p. 3 ([arXiv:astro-ph/0109495](https://arxiv.org/abs/astro-ph/0109495)), [doi:10.1142/9789812811318_0002](https://doi.org/10.1142/9789812811318_0002)
- Rakshit S., Stalin C. S., Kotilainen J., 2020, *ApJS*, **249**, 17
- Richards G. T., et al., 2006, *ApJS*, **166**, 470
- Risaliti G., Lusso E., 2019, *Nature Astronomy*, **3**, 272
- Runoe J. C., Brotherton M. S., Shang Z., 2012, *MNRAS*, **427**, 1800
- Sadowski A., 2011, *arXiv e-prints*, p. [arXiv:1108.0396](https://arxiv.org/abs/1108.0396)
- Secunda A., Jiang Y.-F., Greene J. E., 2024, *ApJ*, **965**, L29
- Sergeev S. G., Doroshenko V. T., Golubinskiy Y. V., Merkulova N. I., Sergeeva E. A., 2005, *ApJ*, **622**, 129
- Shakura N. I., Sunyaev R. A., 1973, *A&A*, **24**, 337
- Shen Y., Ho L. C., 2014, *Nature*, **513**, 210
- Shen Y., Greene J. E., Strauss M. A., Richards G. T., Schneider D. P., 2008, *ApJ*, **680**, 169
- Stone Z., et al., 2022, *MNRAS*, **514**, 164
- Straub O., et al., 2011, *A&A*, **533**, A67
- Tang J.-J., Wolf C., Tonry J., 2023, *Nature Astronomy*, **7**, 473
- Tang J.-J., Wolf C., Tonry J., 2024, *MNRAS*, in press
- Tonry J. L., et al., 2018, *PASP*, **130**, 064505
- Ulrich M.-H., Maraschi L., Urry C. M., 1997, *ARA&A*, **35**, 445
- Uttley P., Edelson R., McHardy I. M., Peterson B. M., Markowitz A., 2003, *ApJ*, **584**, L53
- Vanden Berk D. E., et al., 2004, *ApJ*, **601**, 692
- Wolf C., Lai S., Onken C. A., Amrutha N., Bian F., Hon W. J., Tisserand P., Webster R. L., 2024, *Nature Astronomy*, **8**, 520
- Yu Z., et al., 2020, *ApJS*, **246**, 16
- Zuo W., Wu X.-B., Liu Y.-Q., Jiao C.-L., 2012, *ApJ*, **758**, 104

This paper has been typeset from a $\text{\TeX}/\text{\LaTeX}$ file prepared by the author.

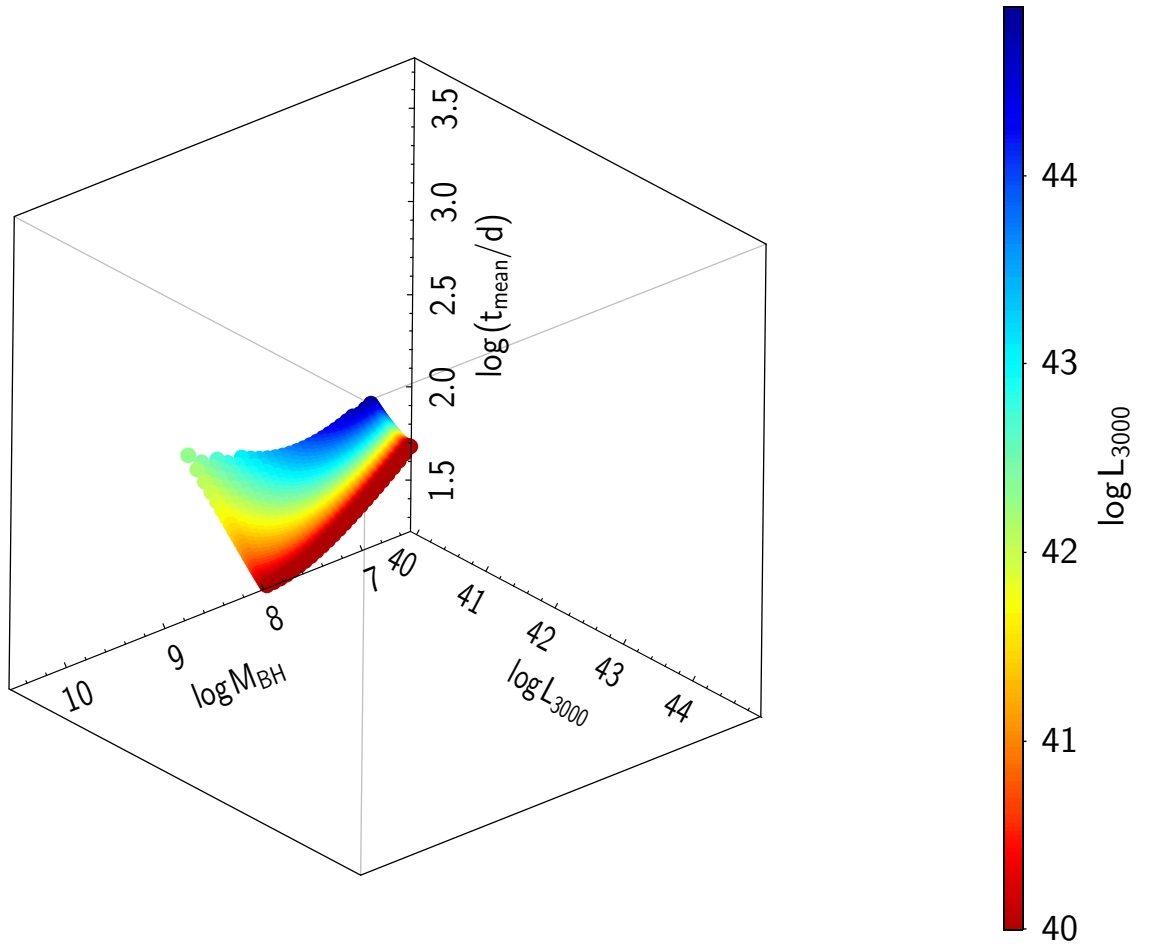


Figure 7. A 3D view of the time scale vs. luminosity and black-hole mass, for a wavelength of 3000\AA , illustrating the curvature of the time-scale plane.